Geometric constraints in the development of primate extrastriate visual cortex

Hyunju Kim[1], Michael J. Arcaro[2], and Nabil Imam[1]

[1]School of Computational Science and Engineering, Georgia Institute of Technology, Atlanta, GA, USA
[2]Department of Psychology, University of Pennsylvania, Philadelphia, PA, USA

Abstract

Although the mechanisms establishing primary sensory maps are well characterized, how multiple higher-order maps with systematic spatial relationships emerge across neocortex remains unclear. Because the probability and strength of cortical connections fall off steeply with distance, cortical geometry may centrally constrain how higher-order maps are arranged. To test this possibility in a well-characterized sensory system, we develop a growth model embedded in the folded surface geometry of the macaque visual cortex, using fMRI-defined V1 retinotopy as the sole functional anchor. Cortical organization emerges through algorithmic growth from primary visual cortex, governed by distance-dependent activity correlations and competition among developing projections. Without imposing areal boundaries, map orientations, or predefined topographic layouts, this process generates multiple retinotopic maps with systematic mirror reversals and smooth gradients that reflect key structural features of fMRI-derived extrastriate maps. Growth parameters estimated from a population template generalize across individual macaques, while individual cortical geometry shapes fine-scale map variation around a shared organizational scaffold. Together, these results show that conserved growth rules acting on realistic cortical geometry produce stereotyped higher-order retinotopic organization under minimal explicit specification.

Introduction

A defining property of neocortex is its organization into orderly topographic maps that preserve spatial continuity, so that nearby points in sensory and motor space are represented by nearby locations on the cortical surface [1–3]. This form of organization is present throughout sensory and motor systems, is conserved across species, and emerges early in development [4–9], suggesting that it is a fundamental feature of cortical wiring and functioning. These maps provide an intrinsic coordinate system that shapes how sensory and motor information propagates across cortex, establishing a spatial framework within which later circuit refinement and functional specializations emerge [3, 10, 11]. While the mechanisms that establish primary maps have been studied extensively [5, 12, 13], it remains unclear how topographic organization is established beyond primary cortex, including the arrangement, orientation, and boundaries of successive maps across higher-order cortex.

Theoretical accounts of cortical organization have argued that such structure can arise from simple developmental rules acting on an intrinsically topographic substrate, rather than from detailed explicit specification of areal identity or map orientation [10, 12, 14–16]. In this view, maps are treated as the primary organizational units of cortex, and complex areal layouts emerge through

self-organizing processes that preserve local continuity while allowing global structure to unfold. Early established topographic maps in primary cortex can therefore act as a stable coordinate system guiding subsequent organization under continuity constraints [10, 17, 18]. From this perspective, mirror-reversing representations that distinguish adjacent maps are not imposed features of areal boundaries but natural consequences of maintaining continuous topography as activity-dependent interactions spread across the cortical sheet [10, 12, 15]. A central prediction of this account is that the arrangement and orientation of maps should follow from conserved growth rules operating on cortical geometry, rather than from explicit instructions specifying boundaries or reversals.

Self-organizing growth models provide a concrete way to formalize and test these ideas. Prior work has shown that simple growth processes combining distance-dependent interactions and wiring constraints can give rise to sequential mirror-reversing maps without imposing areal labels or reversal rules [15, 16]. In these models, higher-order map structure can emerge as an outcome of algorithmic growth initiated from anchor regions, such as the LGN or primary visual cortex, under minimal explicit specification. However, these demonstrations were carried out on simplified substrates, typically planar grids with idealized distance relationships, leaving open the question of whether self-organizing principles operating on real cortical geometry can reproduce higher-order map organization observed in the brain.

This question is particularly important given that cortical connectivity is strongly distance-dependent, with connection probability and strength falling off steeply with physical distance between cortical locations [19, 20]. Interareal projections are additionally shaped by laminar organization and cortical folding, linking surface geometry to long-range connectivity patterns [21,22]. Moreover, developmental growth proceeds on a folded, anisotropic cortical sheet, where much of the increase in connection length reflects stretch-driven expansion of an existing axonal scaffold rather than late formation of new long-range projections [15, 23]. As a result, cortical surface geometry directly constrains which interactions are most likely to occur during development. If distance-dependent interactions and wiring constraints are sufficient to organize higher-order maps, then a growth process embedded in empirically measured cortical geometry should reproduce key features of retinotopic organization observed in the brain without additional specification.

The primate visual system offers an ideal test case for these principles. Multiple retinotopic maps are distributed across occipital and temporal cortex [24–28]. Beyond primary visual cortex, extrastriate areas traditionally labeled V2, V3, and V4 each contain orderly representations of polar angle and eccentricity arranged in a stereotyped spatial layout [10,26,29]. A defining feature of this organization is the presence of mirror-reversing representations at transitions between adjacent maps, in which the progression of visual field representation reverses direction along the cortical surface. This pattern is remarkably reliable across individuals, despite substantial variability in cortical folding and surface geometry [3, 10, 27, 28]. Importantly, this organization is present at birth [9, 30, 31], indicating that it must arise from early developmental processes prior to extensive visual experience.

Here, we derive a distance-based model of cortical development embedded directly within the geometry of the macaque visual cortex, reconstructed from structural and functional MRI. Cortical organization unfolds as a directed growth process from primary visual cortex, governed by activity correlations defined by cortical surface distance together with degree-dependent resource constraints. Without imposing areal boundaries, map orientations, or reversal rules, the model gives rise to multiple orderly retinotopic maps characterized by mirror-reversing phase organization and smooth eccentricity gradients. We apply the same growth rules across population-averaged and individual

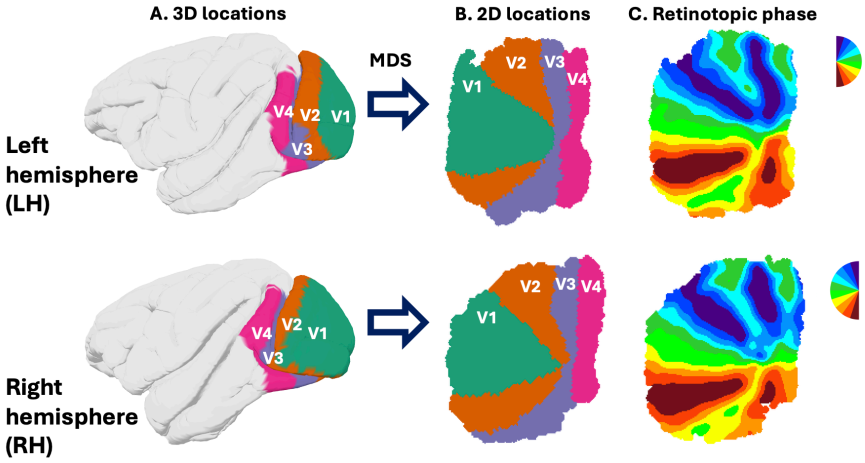

Figure 1: Distance-preserving embedding of the macaque visual cortex. **A.** Three-dimensional cortical surface of the macaque brain from the NIMH Macaque Template (NMT), illustrating the folded geometry of the cortex, with visual areas V1–V4 delineated. **B.** Two-dimensional embedding of cortical locations obtained by multidimensional scaling (MDS), which preserves pairwise distances measured along the folded cortical surface, effectively unfolding the surface geometry of visual cortex into a planar representation. **C.** fMRI-defined retinotopic tuning maps overlaid on the embedded cortical surface. Inset on the right shows the color map of visual space. Top and bottom rows correspond to NMT left and right hemispheres, respectively. For visual comparison, the right hemisphere is mirror reversed to match the orientation of the left hemisphere. Together, the two rows illustrate subtle hemispheric differences in visual area locations and retinotopic map organization that reflect underlying geometric variation in the cortical surface.

macaque cortical surfaces to assess the robustness of emergent map structure and to examine how individual differences in cortical geometry across monkeys shape variation around a shared organizational scaffold. Together, these analyses test whether stereotyped retinotopic organization can emerge through activity-dependent self-organization under minimal explicit specification.

Results

Growth Model Applied to Neocortex. To model cortical map formation under realistic anatomical constraints, growth dynamics were embedded in the folded cortical surface geometry of the macaque visual cortex. The model was formulated as a directed growth process that unfolds in a network, in which nodes represent localized regions sampled from the cortical sheet, each associated with retinotopic tuning measured using functional MRI [7]. Directed edges represent projections originating from primary visual cortex and terminating within a contiguous extrastriate region of visual cortex. Primary analyses were performed on the NIMH Macaque Template (NMT), a population-averaged macaque cortical reference [32], with model simulations conducted separately for the left hemisphere (LH) and right hemisphere (RH). Combined with group average retinotopy, the NMT provides a common anatomical and functional reference frame that captures the typical spatial arrangement of visual maps across individuals. This offers a principled baseline for parameterization and visualization before assessing how individual cortical geometry gives rise to retinotopic organization in individual animals.

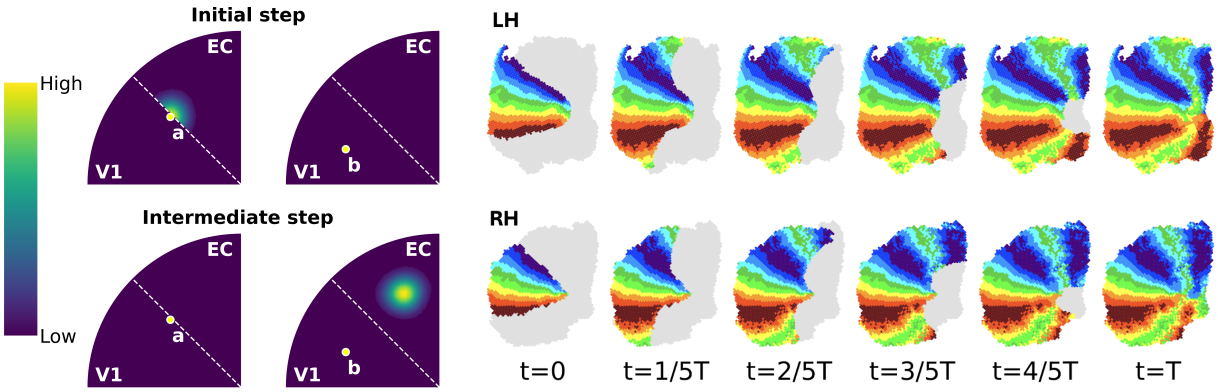

A. Likelihood of new edge **B. Retinotopic phase snapshots**

Figure 2: Development of retinotopic organization in the model. **A.** Illustration of the model. Distance-based activity correlations and degree-dependent competition among V1 nodes (nodes a and b) determine the likelihood of forming new connections with nodes in extrastriate cortex (EC). Brighter colors (yellow) indicate higher probabilities of connection. Initially, distance-dependent correlations favor connections between node a and nearby extrastriate nodes. As connections accumulate, competition for developing connections reshapes the probability landscape, leading connection likelihood to favor node b and more distal extrastriate nodes. Through this self-organizing process, orderly retinotopic organization progressively emerges in extrastriate cortex. **B.** Developmental snapshots of retinotopic phase organization in the model, shown on the NMT surface for the left hemisphere (top) and the right hemisphere (bottom). Colors indicate polar angle representation in contralateral visual space, with red corresponding to the upper vertical meridian, blue to the lower vertical meridian, and green to the horizontal meridian. Across development, organized phase bands emerge and propagate across cortex, exhibiting large-scale mirror-reversing structure.

To allow growth to proceed across the cortical sheet while respecting distances defined by the folded surface, cortical locations were embedded into a two-dimensional coordinate system that preserves distances measured along the cortical surface (Fig. 1, see Methods). This transformation collapses the three-dimensional cortical sheet into a flat representation while preserving intrinsic surface-based relationships, such that nearby cortical locations remain nearby in the embedding despite cortical folding. Accordingly, distances measured between cortical locations in the embedded space were highly correlated with geodesic distances computed on the original cortical surface, with a Spearman rank correlation coefficient of $\rho = 0.992$ for both hemispheres. The resulting distance-preserving representation retained the relative spatial arrangement of primary and higher visual areas and allowed growth dynamics to operate on a continuous two-dimensional cortical sheet derived from real anatomy, rather than on a synthetic grid or volumetric representation.

Cortical map formation was modeled as algorithmic growth, in which directed edges (connections) were progressively added from primary visual cortex to nodes within the extrastriate cortical territory. At each step, candidate edges were evaluated using a growth rule that combines activity-based correlations with a degree-dependent competition term (Fig. 2A, see Methods). Activity correlations favor edges between nodes that are close in distance, whereas the competition term reduces the likelihood that the same primary visual cortex nodes repeatedly form new connections. As edges are added, both activity correlations and competitive weights are updated, dynamically modifying

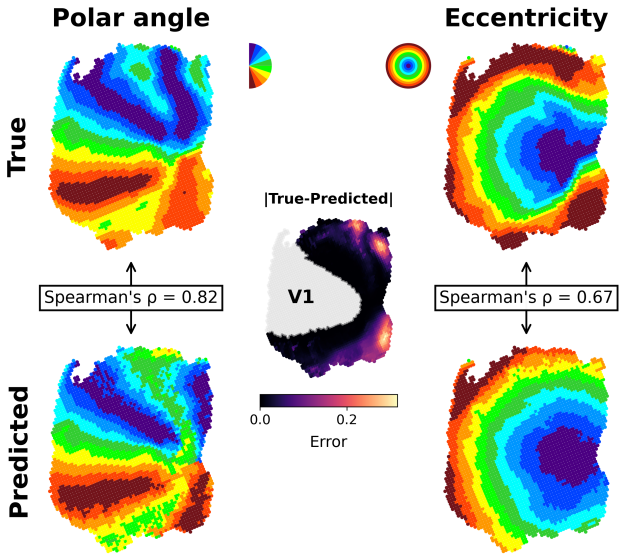

Figure 3: Comparison of true and predicted polar angle and eccentricity maps in NMT left hemisphere. Spearman's ρ calculated pairwise among non-V1 nodes is 0.82 for polar angles, 0.67 for eccentricity. The middle panel shows normalized mean squared error (MSE; scaled 0–1), revealing increasing prediction error with distance from V1. The corresponding result for the right hemisphere is shown in Fig. S1.

pairwise node affinities that govern subsequent edge selection. This interaction between distance-dependent correlations and competition for outgoing connections defines the model mechanism linking cortical surface geometry to emergent retinotopic organization beyond V1.

Emergent Retinotopic Topography in the Template Brain. To assess whether growth constrained by cortical surface geometry is sufficient to generate higher-order retinotopic organization, growth was initiated from primary visual cortex and allowed to unfold across the cortical surface. As growth progressed, extrastriate cortex developed an emergent large-scale topographic organization, with retinotopic phase varying smoothly across the cortical sheet (Fig. 2B). This organization arose incrementally as growth propagated away from V1, demonstrating that surface constrained growth dynamics can give rise to structured retinotopic layouts beyond primary visual cortex.

Across extrastriate cortex, the retinotopic maps generated by the model recapitulated key features of macaque retinotopy spanning areas V2, V3, and V4, measured with fMRI. In model predictions, representations of the lower visual field occupied dorsal extrastriate cortex, while upper visual field representations were located ventrally, reflecting the characteristic inversion of visual space observed in macaque visual cortex (Fig. 3, Fig. S1). Eccentricity organization showed a smooth progression away from the foveal representation, oriented roughly orthogonal to polar angle organization and forming a continuous large-scale gradient that extends in parallel across extrastriate visual areas, in contrast to the mirror reversals observed for polar angle. Quantitatively, polar angle and eccentricity maps in extrastriate cortex exhibited significant correspondence between model predictions and fMRI data, as assessed by rank correlations and by average visual field offsets computed across cortical locations. This correspondence emerged without explicit specification of visual field layout or spatial gradients, arising instead from the growth dynamics acting on the inherited topographic structure of primary visual cortex. Together, these results show that growth constrained by realistic cortical

surface geometry is sufficient to reproduce the large-scale spatial layout of retinotopic organization observed in macaque extrastriate visual cortex.

Mirror-reversing Retinotopic Maps in the Growth Model. In primate visual cortex, boundaries between adjacent extrastriate visual areas are defined by reversals in the progression of polar angle representations along the cortical surface. These reversals mark transitions between distinct retinotopic maps within a continuous topographic organization and provide a functional criterion for identifying map structure independent of anatomical labels.

Consistent with this organizational principle, the emergent topography produced by the growth model exhibited systematic mirror reversals in polar angle representation across extrastriate cortex (Fig. 4). As growth propagated away from primary visual cortex, polar angle representations progressed smoothly over extended cortical regions and then reversed direction at consistent anatomical locations within extrastriate cortex, aligned along the principal axis of propagation. This pattern produced an alternating sequence of polar angle progressions characteristic of multiple retinotopic maps. Notably, these polar angle reversals were not imposed by predefined areal boundaries, map orientations, or reversal rules. Instead, they emerged because the correlation driven growth rule promotes coherent structure both within local extrastriate neighborhoods and in the mapping from V1 inputs onto extrastriate targets. Thus, mirror reversals reflect an emergent property of maintaining smooth topography under surface constrained growth, rather than an explicitly specified feature of the model.

To quantify this organization and compare it directly with empirically measured macaque retinotopy, polar angle phase structure was summarized using an angular periodicity analysis applied to both model-predicted and fMRI-derived maps. For each hemisphere, retinotopic tuning vectors were converted to phase values using the arctangent function and expressed as a function of angular position around the cortical surface. Phase values were sampled across multiple annuli defined at fixed radial spacings and then averaged as a function of polar angle to yield a one-dimensional angular phase profile, capturing the large-scale organization of polar angle representations across the cortical sheet (Fig. 4A). The resulting profiles exhibited clear periodic structure, with local maxima and minima marking points at which the direction of polar angle progression reverses, providing operational markers of transitions between adjacent retinotopic maps (Fig. 4B).

Across hemispheres, angular phase profiles derived from the growth model closely matched those obtained from macaque fMRI data. In both predicted and empirical maps, polar angle representations exhibited phase reversals at comparable angular positions along the cortical surface (Fig. 4B). Specifically, two reversals were observed within the upper visual field representation and two within the lower visual field representation in both model and fMRI profiles. Consistent with this qualitative correspondence, predicted and empirical phase profiles showed strong quantitative agreement, with high circular correlations (LH: $\rho = 0.916$, RH: $\rho = 0.923$) and relatively small mean absolute phase differences (LH: 11.2°, RH: 8.7°). The correspondence in both the number and relative locations of these reversals indicates that the growth model captures not only the overall pattern of polar angle transitions, but also the spatial placement of successive extrastriate maps along the cortical surface as observed in macaque visual cortex. Because these reversal locations define functional boundaries between adjacent retinotopic maps, they were used to estimate the relative surface extent of areas V2, V3, and V4. Model-derived areal extents closely matched those measured from fMRI data for each area and recapitulated the systematic decrease in areal surface area across successive extrastriate maps with increasing map order relative to V1.

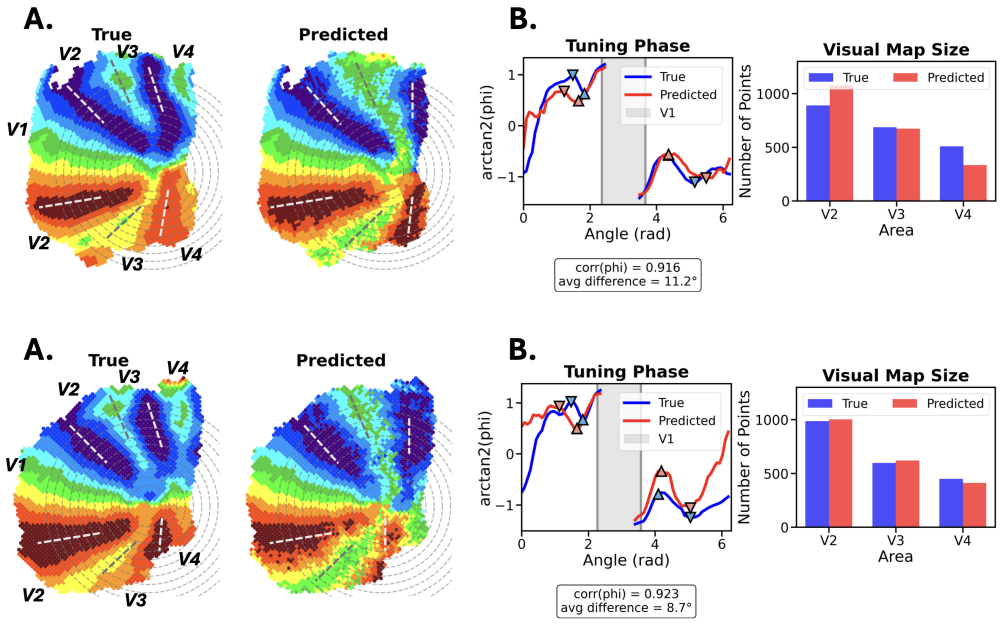

Figure 4: Mirror-reversing retinotopic phase organization and derived visual area boundaries (top: NMT LH, bottom: NMT RH). **A.** Polar angle phase maps for empirically measured macaque fMRI retinotopy and model-predicted organization are shown for each hemisphere, together with inferred boundary locations separating successive mirror-reversing retinotopic maps. **B.** Retinotopic boundaries and area estimation. Boundaries were defined by polar angle phase reversals along the cortical surface, occurring at or near the vertical meridian (dashed white lines) or horizontal meridian (dashed grey lines), and were used to trace retinotopic boundary lines delineating the spatial extent of extrastriate areas V2, V3, and V4, enabling estimation of their relative surface areas. Direct comparison of predicted and empirical boundary locations shows close correspondence in both the placement of map transitions and the relative surface area of each extrastriate visual area.

To assess whether the observed correspondence reflects a specific alignment of retinotopic organization rather than a generic consequence of mirror-reversing structure, we examined the effects of systematically rotating the predicted tuning phase maps prior to comparison with empirical fMRI retinotopy (Fig. 5). Although mirror-reversing boundaries remain evident under rotated configurations, correspondence in the spatial arrangement of polar angle organization was strongest when predicted phase maps were compared without rotation. Quantitatively, this reference alignment produced the highest Spearman rank correlations and lowest mean squared errors across hemispheres. Correspondence declined progressively with increasing rotation, with intermediate rotations (45° and 135°) showing intermediate performance and a 90° rotation yielding the poorest agreement, characterized by strongly reduced or negative correlations and increased error. This pattern indicates that the growth model captures a specific large-scale alignment of retinotopic organization observed in macaque visual cortex, rather than merely reproducing generic features of mirror-reversing map topology.

Cortical Geometry Constrains Individual Retinotopy. Having established that the growth model reproduces the large-scale retinotopic organization observed in macaque visual cortex, the next question was whether differences in cortical geometry further constrain retinotopic maps at the level of individual monkeys. To address this, the growth model was applied independently to each

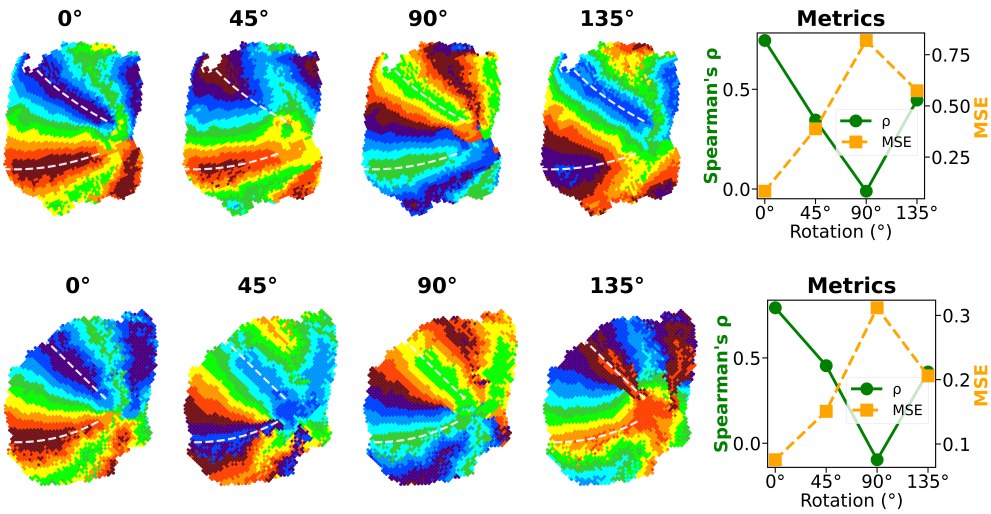

Figure 5: Rotation control for global polar angle phase alignment (top: NMT LH, bottom: NMT RH). Retinotopic phase maps are shown for model predictions after systematically rotating the V1 polar angle phase map (0°, 45°, 90°, 135°) while keeping the growth model and its V1-to-extrastriate connections fixed. For each rotation, predicted extrastriate phase maps were recomputed by propagating the rotated V1 phase values through the model projections, yielding a family of alternative global phase alignments. Although mirror-reversing structure can still emerge under rotation, quantitative correspondence with empirically measured retinotopy is maximal for the unrotated configuration. Summary metrics show Spearman's rank correlation (ρ) and mean squared error (MSE) as a function of rotation angle, with a 90° rotation, corresponding to half of the hemispheric tuning space, yielding the poorest agreement.

macaque dataset using its native cortical surface geometry, while all growth rules and parameters were held fixed across animals. Model predictions were then compared directly with empirically measured retinotopic maps from the same monkeys, allowing evaluation of whether individual cortical folding and surface layout carry information that shapes individual retinotopic organization beyond the population-averaged template.

Across monkeys, the growth model captured features of the individual organization of retinotopic phase observed in the empirical fMRI data (Fig. 6, Fig. S2). In the measured maps, extrastriate visual cortex showed orderly progression of polar angle along the cortical surface, with consistent reversals marking transitions between adjacent retinotopic maps. Predicted eccentricity maps exhibited smooth gradients extending away from the foveal representation that closely aligned with those measured using fMRI. Specifically, Spearman correlations between model-predicted and fMRI-derived maps were consistently high when correlations were first computed separately for the left and right hemispheres and then averaged within each monkey. When summarized across the six monkeys, Spearman correlation values (reported as mean $\pm$ standard deviation) were 0.72 ± 0.04 for polar angle and 0.74 ± 0.06 for eccentricity, reflecting robust individual agreement. Together, these results demonstrate that both angular and radial components of retinotopic organization emerge robustly on individual cortical surfaces and reflect individual deviations beyond a shared, species-typical retinotopic scaffold.

To evaluate whether accurate prediction of individual retinotopic maps depends on the alignment between cortical geometry and V1 tuning statistics, we performed a complementary analysis in which

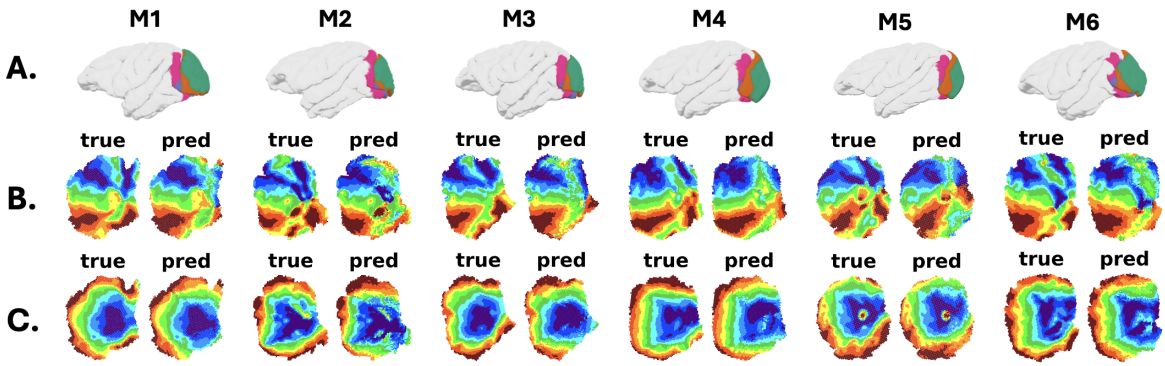

Figure 6: Model predictions across individual cortical geometries. **A.** Three-dimensional cortical surface reconstructions for each dataset, with visual areas V1–V4 indicated by distinct colors, illustrating dataset-specific cortical geometry and areal layout used as the growth substrate. **B.** Retinotopic phase maps, comparing empirically measured maps (true) with model predictions (pred) for the left hemisphere of each monkey. Across datasets, higher visual areas show smooth phase progression within maps and consistent mirror reversals at map boundaries. **C.** Corresponding eccentricity maps showing the radial component of retinotopic organization. The model reproduces individual eccentricity gradients aligned with empirical measurements. The corresponding result for the right hemisphere is shown in Fig. S2.

the growth model was run on each individual macaque cortical surface while substituting V1 tuning statistics from other animals (Fig. 7). For a given monkey, cortical surface geometry and growth parameters were held constant, and only the retinotopic tuning of V1 inputs was exchanged across animals. When tuning statistics from other monkeys were used, the model continued to produce coherent retinotopic organization, indicating that global map structure is strongly constrained by cortical geometry and growth dynamics. However, systematic deviations emerged in fine-scale phase alignment relative to the empirical maps. Correspondence with empirical retinotopy tended to be higher for within-monkey predictions, with most monkeys exhibiting a positive within–cross-monkey difference, a positive mean difference across monkeys, and a reliable bias toward higher within-monkey correspondence confirmed by an exact one-sided sign-flip test that enumerates all 2^6 possible sign assignments under the null hypothesis of zero mean advantage ($p = 0.0312$). Together, these results indicate that the structure of extrastriate retinotopic organization is strongly shaped by geometric features shared across macaque cortices, while individual differences in cortical geometry systematically modulate this structure to produce monkey specific connectivity patterns.

Discussion

We show that higher-order retinotopic organization can emerge from growth dynamics constrained by realistic cortical surface geometry. When embedded within folded macaque cortical anatomy and initiated from primary visual cortex, a distance-dependent growth process generated smooth retinotopic gradients, systematic mirror reversals in polar angle, and spatial layouts that closely match retinotopic organization measured using macaque fMRI. These results demonstrate that large-scale extrastriate map organization, including the relative placement of multiple retinotopic maps, can arise without explicit specification of visual area boundaries, map orientations, or reversal locations. Instead, this pattern follows from conserved growth rules acting on the folded cortical

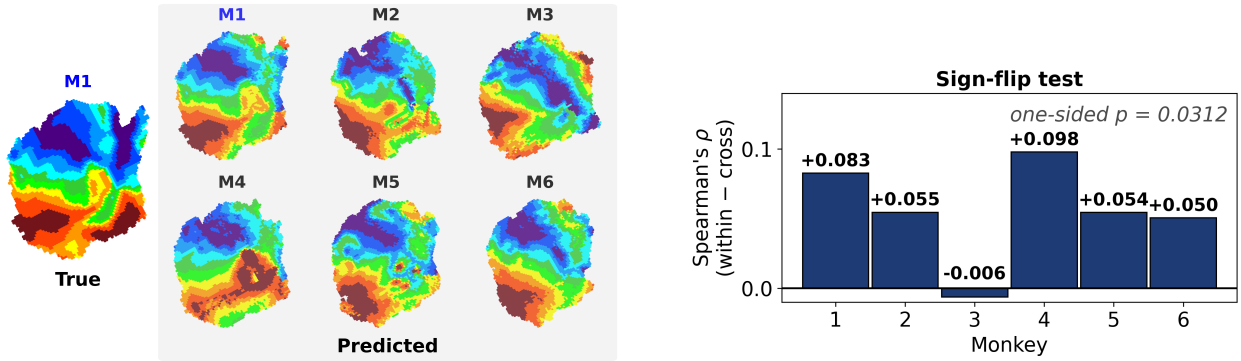

A. Tuning transfer across monkeys

B. Individual prediction advantage across monkeys

Figure 7: Contribution of cortical geometry and tuning statistics to individual retinotopic predictions. **A.** Retinotopic phase maps projected onto the cortical surface of a representative monkey (M1 LH), comparing empirically measured polar angle maps with model predictions generated using cross-monkey V1 tuning statistics from other monkeys (M2–6 LH). Across tuning sources, the model produces coherent retinotopic layouts, while fine-scale phase alignment varies depending on the match between tuning statistics and cortical geometry. **B.** Difference in correspondence between predicted and empirical retinotopy for within-monkey versus cross-monkey predictions across individual monkeys. Most monkeys show higher correspondence for within-monkey predictions, with one monkey exhibiting a small effect in the opposite direction. The mean within–cross-monkey difference across monkeys is positive, and a one-sided sign-flip test indicates a reliable bias toward higher within-monkey correspondence ($p = 0.0312$).

sheet together with inherited topographic structure from primary visual cortex.

Primary Cortical Anchors and Emergent Map Organization. These results support theoretical accounts in which early established topographic maps in primary cortex act as developmental anchors for subsequent cortical organization. In primates, primary visual cortex provides a stable retinotopic coordinate system that constrains the emergence of higher-order maps through continuity-preserving growth dynamics [3, 10]. Within this framework, mirror-reversing representations are not imposed markers of areal identity but arise naturally from extending continuous topography across the cortical surface under distance-constrained interactions [15]. The present model formalizes this idea within measured cortical surface geometry, demonstrating that mirror reversals emerge from correlation-driven growth and competition among developing projections. Together, these factors generate coherent structure within extrastriate neighborhoods, defined by the the mapping from primary visual cortex onto extrastriate targets, without requiring explicit boundaries or reversal rules.

Prior modeling work has shown that continuity and competition are, in principle, sufficient to generate higher-order retinotopic structure. Broadly, these models fall into two categories: algorithmic growth models, in which mirror-reversing maps emerge from developmental wiring rules [15, 16], and optimization-based models, in which higher-order spatial structure arises once model parameters are optimized for functional objectives [33, 34]. Both approaches, however, have either assumed idealized geometry or fixed areal layouts, leaving unresolved how real cortical anatomy shapes the emergence and placement of retinotopic maps across cortex. The present results address this gap by showing

that cortical geometry plays an active role in shaping continuity-based organization, constraining the emergence and placement of retinotopic maps across cortex. When growth dynamics is embedded in measured macaque cortical surfaces, the resulting retinotopic maps reproduce the spatial layout observed with fMRI, with individual differences in cortical folding predicting individual differences in map arrangement around a shared organizational scaffold. Together, these results suggest a division of roles: continuity and competition define the space of possible organizational motifs, while cortical geometry constrains which configurations can be realized in each brain.

The anchoring framework used here also highlights important limits. When multiple anchors converge within the same cortical territory, continuity constraints may conflict, leading to local discontinuities in topographic structure [10, 35]. In addition, the influence of primary sensory anchors may weaken with increasing distance from early sensory cortex, allowing greater flexibility in higher-order regions [36]. The present model supports this view—correspondence between predicted and empirically measured retinotopic organization systematically decreased with increasing distance from V1, as reflected by rising prediction error from V2 to V3 to V4. This pattern parallels prior empirical findings showing a decrease in spatial correlation between extrastriate visual areas and V1 at increasing cortical distances [37]. Together, these results suggest that early extrastriate organization remains strongly anchored to primary cortex, whereas reduced anchoring at greater distances may permit increased variability in areal size, layout, and functional specialization. Extending the present model to incorporate multiple anchors or pathway-specific growth rules may therefore be necessary to explain organization beyond early extrastriate areas tested in the current study, particularly where retinotopic maps diverge across parallel processing streams.

Generalization across Individuals and Species. A central finding of this study is that the same growth rules reproduce retinotopic organization across individual macaques when applied to each animal's native cortical geometry. Despite substantial inter-individual variability in cortical folding and surface layout, the model captures the spatial arrangement of retinotopic maps observed in each monkey, indicating that individual differences in cortical geometry constrain how retinotopic organization is expressed beyond a shared species-typical scaffold [7, 24].

Evaluating whether these principles extend beyond macaques is important for two related reasons. First, the substantial differences in scale and systems-level organization between human and macaque visual cortex provide a strong test of whether shared geometry-constrained growth rules can generate distinct map organizations across species. Second, the successful application of the same model to multiple primate species carries implications for developmental timing. Large-scale resting-state fMRI studies show that human visual cortex is already organized at birth into distinct pathways with posterior-to-anterior hierarchical structure and adult-like topographic organization, and that this organization strengthens across late gestation [38]. In macaques, retinotopic proto-organization is likewise present at or near birth [7]. If growth dynamics can account for map organization in both humans and macaques, this would explain the early emergence of retinotopic organization in both species prior to extensive postnatal experience.

Cross-species comparisons also clarify which aspects of retinotopic organization generalize as the cortex expands. Continuity-based models suggest that increasing cortical surface area can yield additional mirror-reversing maps as cortex is filled in under smoothness constraints [15]. This is motivated by empirical work proposing a roughly 10-fold increase in the number of cortical areas from early mammals to primates [14, 39]. However, in primates, cortical surface expansion does not necessarily translate into a greater number of early retinotopic maps. Recent work comparing

macaques and humans argues that primate visual cortex evolution is dominated by expansion of a conserved architectural scaffold rather than proliferation of new early maps [37]. Applying geometry-constrained growth models to human cortical surfaces therefore provides a direct test of whether conserved developmental rules predict conserved map number while allowing species differences to emerge in map spacing and pathway organization, consistent with network-level perspectives emphasizing distributed and interacting pathways [40].

Developmental Timing and Anatomical Constraints. The growth model used here was embedded in cortical geometries derived from adult macaque brains, even though retinotopic maps emerge very early in development. In macaques, large-scale retinotopic organization is already present at or near birth, with orderly polar angle and eccentricity gradients observed across visual cortex prior to extensive visual experience [7]. Although the cortex expands substantially after birth, available evidence suggests that this expansion preserves the relative spatial organization of visual cortex. Despite large increases in cortical surface area across development, the proportional arrangement of visual areas relative to primary visual cortex remains stable [37]. These observations support the use of adult cortical geometry as a reasonable approximation of the anatomical constraints relevant for early map formation, while motivating future work embedding the model in fetal or neonatal cortical reconstructions.

Limitations and Future Work. A limitation of the present model concerns how interaction structure is defined. Activity correlations were parameterized using distances measured along the cortical surface, which capture key spatial constraints imposed by the folded cortical sheet; however, true axonal path lengths traverse white matter and may diverge from surface geodesic distance. Moreover, cortical folding itself likely reflects developmental constraints imposed by connectivity rather than serving as a purely independent substrate [23]. While surface distance is therefore a reasonable proxy for relative interaction strength across much of visual cortex, especially for short- and intermediate-range connections, exploring alternative distance formulations, including unfolded geometries or tract-informed measures, would help clarify which aspects of cortical geometry are most critical for map spacing and layout. The model also treats cortical nodes as uniform units, despite known variation in neuronal density, receptive field size, and representational scale across visual areas. Incorporating area-dependent heterogeneity will yield a more biologically-grounded account of how map spacing and transition sharpness vary along the visual hierarchy. Finally, growth in the present model is seeded directly from primary visual cortex rather than proceeding through an explicitly hierarchical sequence of interareal stages. Although mirror-reversing organization does not require a hierarchical growth rule, comparing direct and staged growth formulations may further clarify how anatomical connectivity and developmental timing jointly shape higher-order map organization.

Implications for Cortical Area Formation. More broadly, these results support theories of cortical map formation in which areas emerge as stable patterns within a continuous topographic field rather than as discrete units requiring explicit specification of areal boundaries [3,10,15]. In this framework, mirror-reversing structure reflects transitions in map orientation that arise naturally from continuity-preserving dynamics on a folded surface, and map boundaries can be defined operationally from intrinsic organization rather than from predefined labels. The present model contributes a mechanistic link between realistic cortical geometry and the emergence and placement of multiple retinotopic maps. Together with recent accounts of functional organization at multiple stages of the visual hierarchy [33,34], these results suggest that wiring, geometry, and growth dynamics jointly shape how cortical maps emerge, stabilize, and diversify across individuals and species.

Methods

Data Acquisition. Retinotopic mapping data were acquired from six macaque monkeys using a 3T TimTrio scanner with a 4-channel surface coil at the Athinoula A. Martinos Center for Biomedical Imaging, Massachusetts General Hospital. Functional images were collected using an EPI sequence at 1 mm isotropic resolution. High-resolution anatomical images were acquired with a 3T Siemens Skyra scanner using a 16-channel knee coil at Brigham and Women's Hospital, with MPRAGE sequences at 0.5 mm isotropic resolution. Additional acquisition details are provided in [30].

Retinotopic mapping was conducted using standard traveling-wave paradigms with flickering checkerboard stimuli. Polar angle mapping utilized a rotating wedge stimulus, while eccentricity mapping employed an expanding or contracting annulus, both centered on a fixation point. Polar angle and eccentricity maps were projected onto each monkey's reconstructed cortical surfaces. Borders between visual maps were delineated by reversals in polar angle representation at or near the horizontal, upper vertical, and/or lower vertical meridian. Full methodological details are available in prior publication [7]. For each monkey, retinotopic measurements were obtained separately for the left and right hemispheres, yielding a total of 12 hemispheres. Cortical surfaces were parcellated into nodes of approximately 1 mm^2, and analyses were restricted to visual areas V1–V4. Each node was associated with its cortical spatial coordinates and a two-dimensional retinotopic tuning vector derived from fMRI responses. Individual hemisphere datasets are denoted using individual identifiers (M1–M6) and hemisphere labels (LH, RH), where LH and RH refer to the left and right hemispheres, respectively. Primary analyses were performed on the NMT geometry.

Cortical Surface Geometry and Distance Metrics. The growth model requires estimates of interaction strength between cortical locations, which depend on the distances separating them. Local intra-areal connectivity within gray matter tracks closely with distance along the cortical surface, while inter-areal projections traverse white matter pathways. Methods to accurately measure distances along these inter-areal fiber tracts are not established; however, relative distances along white matter pathways largely reflect relative distances along the cortical surface. We therefore used cortical surface distance as a proxy for the spatial constraints governing both local and long-range interactions in the growth model.

Cortical surface distances were computed nodewise between all surface nodes within a region of visual cortex encompassing areas V1, V2, V3, and V4. For each monkey and hemisphere, geodesic distances were computed along both the pial and smoothed white matter surface reconstructions using AFNI's SurfDist. Distances computed on the pial and white matter surfaces were averaged to obtain a single cortical surface distance estimate for each node pair, providing a robust measure that accounts for folding-related differences between surface representations.

To obtain a uniformly sampled representation of cortex while preserving its intrinsic geometry, three-dimensional cortical coordinates were embedded into two dimensions using multidimensional scaling (MDS). The MDS embedding was computed directly from the full nodewise cortical distance matrix and preserved relative distances between node pairs, with Pearson correlations between cortical surface distances and Euclidean distances in the 2D embedding exceeding 0.99. This distance-preserving embedding provides a flattened representation of the cortical sheet that retains intrinsic spatial relationships imposed by cortical geometry.

The embedding was resampled onto a uniformly spaced grid and the 2D Euclidean retinotopic tuning coordinates were smoothed and interpolated using Matérn-kernel Gaussian process regression

($\nu = 2.5$, length scale = 1.0, noise level = 0.1), with the two coordinate dimensions fit separately [41]. Each grid location was treated as a node in the network, forming the substrate for subsequent growth simulations. The resulting network comprised 3,486 nodes in NMT LH (1,334 in primary visual cortex and 2,152 in higher visual areas) and 3,238 nodes in NMT RH (1,110 in primary visual cortex and 2,128 in higher visual areas). Each node inherits both its position along the cortical surface and its retinotopic tuning from the underlying imaging data.

Activity Correlation. Pairwise activity correlations between nodes were defined as a function of distance in the two-dimensional MDS embedding. For any pair of nodes u and v, distance was expressed in polar coordinates relative to a common foveal reference point, decomposed into radial distance and angular distance.

Radial proximity was quantified by the absolute difference in radial distance from the foveal center. Let r_u and r_v denote the radial coordinates of nodes u and v in the MDS embedding. The radial distance was defined as

$$\Delta r(u, v) = |r_u - r_v|. \tag{1}$$

Angular proximity was quantified by the circular distance in polar angle around the foveal center. Let θ_u and θ_v denote the polar angles of nodes u and v. The angular distance was defined as

$$\Delta\theta(u, v) = \min(|\theta_u - \theta_v|,\ 2\pi - |\theta_u - \theta_v|)\,. \tag{2}$$

Both distance measures were converted into similarity kernels using Gaussian functions,

$$\begin{aligned} d_{\mathrm{R}}(u, v) &= \exp\left(-\frac{\Delta r(u, v)}{\sigma_{\mathrm{R}}}\right), \\ d_{\mathrm{A}}(u, v) &= \exp\left(-\frac{\Delta\theta(u, v)}{\sigma_A}\right), \end{aligned} \tag{3}$$

where σ_{R} and σ_A control the radial and angular scales, respectively. The resulting coactivation strength between nodes u and v was defined as

$$d(u, v) = d_{\mathrm{R}}(u, v)\, d_{\mathrm{A}}(u, v), \tag{4}$$

so that strong coactivation occurred only among nodes that were physically proximal in the embedding.

Using this fixed coactivation kernel, the activity correlation between a V1 node u and an extrastriate node v was defined as

$$c(u, v) = d(u, v) + \sum_{(i,j)\in E} d(u, i)\, d(j, v), \tag{5}$$

where E denotes the current set of directed edges. The second term captures indirect correlations mediated by existing projections.

Degree-dependent Competition. This term captures competition among V1 nodes for outgoing connections. As the out-degree of a V1 node increases during network growth, its competitive weight decreases according to the degree-dependent competition term described below.

For a V1 node u, a normalized out-degree was first computed before each growth step,

$$\hat{k}_u = \frac{k_u}{\max_{v \in \mathrm{V1}} k_v + 1}, \tag{6}$$

where k_u denotes the out-degree of node u.

Based on the normalized degree $\hat{k}_u$, the competition weight was defined as

$$\gamma(u) = 0.2 + 0.8 \left(1 - \hat{k}_u\right)^2, \tag{7}$$

which is a monotonically decreasing and strictly positive function of degree. This formulation assigns lower competitive strength to highly connected nodes while maintaining a constant baseline level of competition for all nodes.

Network Growth. The network grew by sequentially adding directed edges from nodes in V1 to nodes in extrastriate cortex, forming a directed bipartite architecture starting from an initially unconnected graph. At each growth iteration, an affinity score was computed between each V1 node and each unconnected extrastriate node (i.e. an extrastriate node that has not yet connected to the bipartite architecture),

$$s(u, v) = c(u, v)\ \gamma(u), \tag{8}$$

where $s(u, v)$ denotes the affinity score between V1 node u and extrastriate node v, $c(u, v)$ is the activity correlation between the two nodes (Eq. 5), and $\gamma(u)$ is the competitive weight of node u (Eq. 7). The score quantified node u's propensity to connect to node v [15]. After computing the affinities between each V1 node and each unconnected extrastriate node, all unconnected extrastriate nodes were ranked by their maximal affinities.

For each selected target node v, the V1 source node with which it had the highest affinity was selected, and a directed edge was added accordingly. The number of target nodes selected at each growth step was initialized to the number of nodes along the V1 boundary and linearly decreased across growth steps. After each edge addition, the activity correlation and degree-dependent competition terms were updated.

Parameter Settings. The model has only two free parameters: the radial and angular components of the activity correlation kernel (σ_R and σ_A respectively in Eq. 3), which determine the spatial extent of activity correlations on the cortical surface. These parameters were tuned to match the retinotopic tuning values observed in the NMT dataset and were held fixed across the individual datasets. The radial component was set to $\sigma_R = 1$ for both hemispheres. The angular component was set to $\sigma_A = 11.5$ for the left hemisphere and $\sigma_A = 13.0$ for the right hemisphere. Effects of varying these parameters are shown in Fig. S3.

Quantitative Comparison of Predicted and Empirical Maps. Model predictions were compared with empirically measured retinotopic maps using Spearman rank correlations computed separately for polar angle and eccentricity. Analyses were restricted to extrastriate nodes (V2–V4) to assess prediction accuracy beyond the V1 anchor. Polar angle values were represented as arctangent-derived phase angles prior to comparison, and circular wrap-around was handled by expressing phase differences on the minimal angular distance. Except when angular and eccentricity correlations were analyzed individually, the two Spearman correlation values were averaged to yield a single summary measure of rank-based prediction accuracy.

Mean squared error (MSE) was computed as the average squared difference between predicted and empirical retinotopic coordinates across nodes. Prediction error was calculated in two-dimensional retinotopic space using normalized x and y coordinates. Coordinate values were normalized to the range $[0, 1]$ within each hemisphere prior to error computation. To visualize spatial patterns of prediction accuracy, MSE was also computed separately for each node and mapped onto the cortical surface.

Angular Phase Analysis and Boundary Detection. To quantify the periodic structure of polar angle representations, retinotopic tuning vectors were converted to phase values using the two-argument arctangent function, yielding phase angles in the range $[-\pi, \pi]$. Phase values were sampled across multiple thin annuli in the MDS space, with ring centers at fixed radii $r = 5, 7, 9, \ldots, 25$, and evaluated over angular positions spanning 0°–360° at 5° increments. For each annulus, phase values were averaged within a combined radial and angular window (radial half-width ± 0.8; angular half-width $\pm 5°$), and the resulting phase curves were averaged across annuli.

For each hemisphere, phase values within the annulus were grouped by angular position around the cortical surface, defined relative to the foveal center in the two-dimensional cortical embedding. Phase values were averaged within uniformly spaced angular bins using circular means to obtain a one-dimensional angular phase profile. The resulting profile was lightly smoothed to reduce local noise while preserving large-scale structure.

Local maxima and minima in the angular phase profile were identified as points at which the direction of polar angle progression reverses, providing operational markers of boundaries between adjacent retinotopic maps. Boundary lines were traced on the cortical surface by following iso phase contours corresponding to these reversal points, yielding estimates of the spatial extent and relative surface area of extrastriate visual areas.

Rotation Analysis. To assess whether correspondence between predicted and empirical retinotopy reflects specific alignment of retinotopic organization or generic mirror-reversing structure, V1 polar angle phase values were systematically rotated by fixed offsets (0°, 45°, 90°, 135°) prior to propagation through the model. Rotations were implemented as additive phase offsets applied to V1 polar angle values, with phase values wrapped to the original angular range after rotation.

For each rotation, extrastriate polar angle phase predictions were recomputed by applying the fixed V1-to-extrastriate projection weights obtained from the unrotated growth model; growth dynamics and connectivity were not rerun. Eccentricity values and all model parameters were held fixed. Spearman rank correlations and mean squared error were then computed between rotated predictions and empirically measured retinotopy, restricted to extrastriate nodes and using the same circular and normalization procedures as in the primary quantitative analyses.

Cross-monkey Generalization Analysis. To evaluate the relative contribution of individual cortical geometry and V1 tuning statistics across monkeys, the growth model was applied to each monkey's native cortical surface geometry while systematically substituting V1 retinotopic tuning from other monkeys.

For each target monkey, growth was performed on that monkey's native cortical surface geometry using identical growth parameters. Model predictions were generated under two conditions: (1) using monkey-matched V1 retinotopic tuning and (2) using V1 tuning transferred from each of the remaining five monkeys, with tuning transferred between homologous hemispheres.

Prediction accuracy was quantified by Spearman rank correlation between predicted and empirically measured retinotopy, computed separately for polar angle and eccentricity and restricted to extrastriate nodes (V2—V4). For each monkey, prediction accuracy was summarized across hemispheres. A sign test assessed whether within-monkey predictions systematically outperformed cross-monkey predictions: under the null hypothesis that within- and cross-monkey predictions are equally likely to yield higher correspondence, the probability that all six monkeys exhibit higher within-monkey correspondence is $1/2^6 \approx 0.016$.

Statistical Analyses. Statistical analyses were used to quantify correspondence between model-predicted and empirically measured retinotopic organization and to assess monkey specificity of model predictions. Agreement between predicted and empirical polar angle and eccentricity maps was quantified using Spearman rank correlation, computed separately for each tuning dimension and restricted to extrastriate cortical nodes (V2—V4) to evaluate performance beyond the V1 anchor. Prediction error was additionally quantified using mean squared error (MSE), computed per node and averaged across nodes, based on squared error in normalized two-dimensional retinotopic coordinates (x and y). Spearman rank correlations were computed separately for polar angle and eccentricity. Nodewise MSE values were also visualized on the cortical surface to assess spatial patterns of prediction accuracy. Individual Specificity in cross-monkey generalization analyses was evaluated using a sign test comparing within-monkey and cross-monkey prediction accuracy across monkeys. No parametric assumptions were made about error distributions, and no correction for multiple comparisons was required because each statistical test addressed a distinct, predefined analysis objective.

References

[1] Vernon B Mountcastle. Modality and topographic properties of single neurons of cat's somatic sensory cortex. *Journal of neurophysiology*, 20(4):408–434, 1957.

[2] David H Hubel and Torsten N Wiesel. Receptive fields, binocular interaction and functional architecture in the cat's visual cortex. *The Journal of physiology*, 160(1):106, 1962.

[3] Jon H Kaas. Evolution of columns, modules, and domains in the neocortex of primates. *Proceedings of the National Academy of Sciences*, 109:10655–10660, 2012.

[4] Larry C Katz and Carla J Shatz. Synaptic activity and the construction of cortical circuits. *Science*, 274(5290):1133–1138, 1996.

[5] Dennis DM O'Leary, Shen-Ju Chou, and Setsuko Sahara. Area patterning of the mammalian cortex. *Neuron*, 56(2):252–269, 2007.

[6] Jianhua Cang and David A Feldheim. Developmental mechanisms of topographic map formation and alignment. *Annual review of neuroscience*, 36(1):51–77, 2013.

[7] Michael J Arcaro and Margaret S Livingstone. Retinotopic organization of scene areas in macaque inferior temporal cortex. *Journal of Neuroscience*, 37(31):7373–7389, 2017.

[8] Nabil Imam, Matthew Kielo, Brandon M Trude, and Barbara L Finlay. Dual computational systems in the development and evolution of mammalian brains. *bioRxiv*, pages 2024–11, 2024.

[9] Michael Arcaro and Margaret Livingstone. A whole-brain topographic ontology. *Annual Review of Neuroscience*, 47, 2024.

[10] Marcello GP Rosa. Visual maps in the adult primate cerebral cortex: some implications for brain development and evolution. *Brazilian Journal of Medical and Biological Research*, 35:1485–1498, 2002.

[11] Michael J Arcaro and Margaret S Livingstone. On the relationship between maps and domains in inferotemporal cortex. *Nature Reviews Neuroscience*, 22(9):573–583, 2021.

[12] Geoffrey J Goodhill. Mathematical guidance for axons. *Trends in neurosciences*, 21(6):226–231, 1998.

[13] Lowry A Kirkby, Georgeann S Sack, Alana Firl, and Marla B Feller. A role for correlated spontaneous activity in the assembly of neural circuits. *Neuron*, 80(5):1129–1144, 2013.

[14] Jon H Kaas. Reconstructing the areal organization of the neocortex of the first mammals. *Brain Behavior and Evolution*, 78(1):7–21, 2011.

[15] Nabil Imam and Barbara L. Finlay. Self-organization of cortical areas in the development and evolution of neocortex. *Proceedings of the National Academy of Sciences*, 117(46):29212–29220, 2020.

[16] Sarthak Chandra, Mikail Khona, Talia Konkle, and Ila R Fiete. Self-organized emergence of modularity, hierarchy, and mirror reversals from competitive synaptic growth in a developmental model of the visual pathway. *bioRxiv*, pages 2024–01, 2024.

[17] Marcy A Kingsbury and Barbara L Finlay. The cortex in multidimensional space: where do cortical areas come from? *Developmental Science*, 4(2):125–142, 2001.

[18] Leah Krubitzer. The organization of neocortex in mammals: are species differences really so different? *Trends in neurosciences*, 18(9):408–417, 1995.

[19] MP Young, JW Scannell, MA O'Neill, CC Hilgetag, GAPC Burns, and C Blakemore. Non-metric multidimensional scaling in the analysis of neuroanatomical connection data and the organization of the primate cortical visual system. *Philosophical Transactions of the Royal Society of London. Series B: Biological Sciences*, 348(1325):281–308, 1995.

[20] Bernhard Hellwig. A quantitative analysis of the local connectivity between pyramidal neurons in layers 2/3 of the rat visual cortex. *Biological cybernetics*, 82(2):111–121, 2000.

[21] Claus C Hilgetag and Helen Barbas. Developmental mechanics of the primate cerebral cortex. *Anatomy and embryology*, 210(5):411–417, 2005.

[22] Claus C Hilgetag and Helen Barbas. Role of mechanical factors in the morphology of the primate cerebral cortex. *PLoS computational biology*, 2(3):e22, 2006.

[23] David C van Essen. A tension-based theory of morphogenesis and compact wiring in the central nervous system. *Nature*, 385(6614):313–318, 1997.

[24] David C Van Essen, William T Newsome, and John HR Maunsell. The visual field representation in striate cortex of the macaque monkey: asymmetries, anisotropies, and individual variability. *Vision research*, 24(5):429–448, 1984.

[25] Martin I Sereno, Anders M Dale, John B Reppas, Kenneth K Kwong, John W Belliveau, Thomas J Brady, Bruce R Rosen, and Roger B H Tootell. Borders of multiple visual areas in humans revealed by functional magnetic resonance imaging. *Science*, 268(5212):889–893, 1995.

[26] Brian A Wandell, Serge O Dumoulin, and Alyssa A Brewer. Visual field maps in human cortex. *Neuron*, 56(2):366–383, 2007.

[27] Thomas Janssens, Qi Zhu, Ivo D Popivanov, and Wim Vanduffel. Probabilistic and single-subject retinotopic maps reveal the topographic organization of face patches in the macaque cortex. *Journal of Neuroscience*, 34(31):10156–10167, 2014.

[28] Liang Wang, Ryan EB Mruczek, Michael J Arcaro, and Sabine Kastner. Probabilistic maps of visual topography in human cortex. *Cerebral cortex*, 25(10):3911–3931, 2015.

[29] Michael J Arcaro and Sabine Kastner. Topographic organization of areas v3 and v4 and its relation tosupra-areal organization of the primate visual system. *Visual neuroscience*, 32:E014, 2015.

[30] Michael J Arcaro and Margaret S Livingstone. A hierarchical, retinotopic proto-organization of the primate visual system at birth. *Elife*, 6:e26196, 2017.

[31] Michael J Arcaro, Peter F Schade, and Margaret S Livingstone. Universal mechanisms and the development of the face network: what you see is what you get. *Annual review of vision science*, 5(1):341–372, 2019.

[32] Benjamin Jung, Paul A Taylor, Jakob Seidlitz, Caleb Sponheim, Pierce Perkins, Leslie G Ungerleider, Daniel Glen, and Adam Messinger. A comprehensive macaque fmri pipeline and hierarchical atlas. *Neuroimage*, 235:117997, 2021.

[33] Eshed Margalit, Hyodong Lee, Dawn Finzi, James J DiCarlo, Kalanit Grill-Spector, and Daniel LK Yamins. A unifying framework for functional organization in early and higher ventral visual cortex. *Neuron*, 112(14):2435–2451, 2024.

[34] Nicholas M Blauch, Marlene Behrmann, and David C Plaut. A connectivity-constrained computational account of topographic organization in primate high-level visual cortex. *Proceedings of the National Academy of Sciences*, 119(3):e2112566119, 2022.

[35] Hsin-Hao Yu, Declan P Rowley, Nicholas SC Price, Marcello GP Rosa, and Elizabeth Zavitz. A twisted visual field map in the primate dorsomedial cortex predicted by topographic continuity. *Science advances*, 6(44):eaaz8673, 2020.

[36] Randy L Buckner and Fenna M Krienen. The evolution of distributed association networks in the human brain. *Trends in cognitive sciences*, 17(12):648–665, 2013.

[37] Emily E Meyer, Marcelina Martynek, Sabine Kastner, Margaret S Livingstone, and Michael J Arcaro. Expansion of a conserved architecture drives the evolution of the primate visual cortex.

Proceedings of the National Academy of Sciences, 122(3):e2421585122, 2025.

[38] Vladislav Ayzenberg and Michael Arcaro. Functional organization of the human visual system at birth and across late gestation. *bioRxiv*, pages 2025–09, 2025.

[39] Leah Krubitzer. In search of a unifying theory of complex brain evolution. *Annals of the new York Academy of Sciences*, 1156(1):44–67, 2009.

[40] James A Bourne, Radoslaw M Cichy, Lynne Kiorpes, Maria Concetta Morrone, Michael J Arcaro, and Kristina J Nielsen. Development of higher-level vision: A network perspective. *Journal of Neuroscience*, 44(40), 2024.

[41] Christopher K. I. Williams and Carl Edward Rasmussen. *Gaussian Processes for Machine Learning*. MIT Press, Cambridge, MA, 2006.

Supplementary Materials

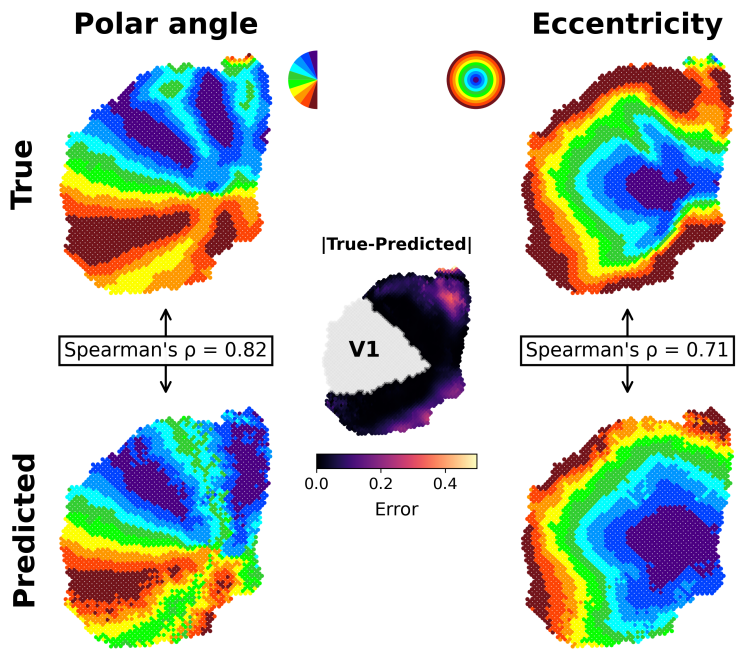

Figure S1: Comparison of true and predicted polar angle and eccentricity maps in NMT LH. Non-V1 Spearman's $\rho = 0.82$ for polar angles, $\rho = 0.71$ for eccentricity. The middle panel shows normalized mean squared error (MSE; scaled 0–1), revealing increasing prediction error with distance from V1.

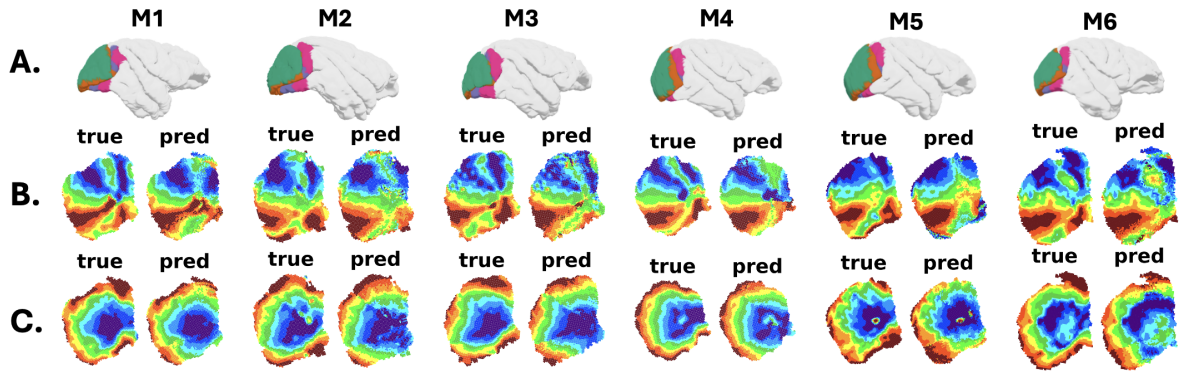

Figure S2: Model predictions across individual cortical geometries in the right hemisphere. **A.** Three-dimensional cortical surface reconstructions for each dataset, with visual areas V1–V4 indicated by distinct colors, illustrating dataset-specific cortical geometry and areal layout used as the growth substrate. **B.** Retinotopic phase maps, comparing empirically measured maps (true) with model predictions (pred) for each monkey. Across datasets, higher visual areas show smooth phase progression within maps and consistent mirror reversals at map boundaries. **C.** Corresponding eccentricity maps showing the radial component of retinotopic organization. The model reproduces monkey-specific eccentricity gradients aligned with empirical measurements.

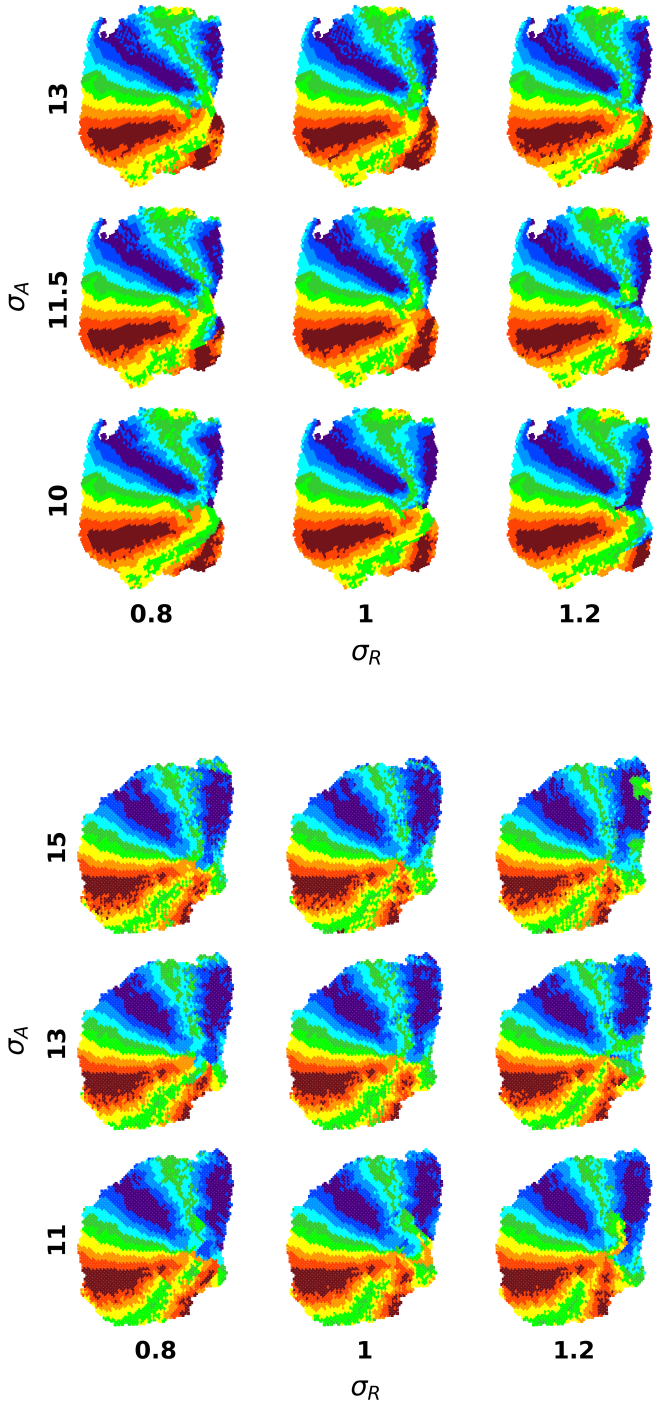

Figure S3: Effects of varying the two parameters of the model (σ_R and σ_A) for NMT left hemisphere (top) and NMT right hemisphere (bottom). The values of these parameters determine the spatial extent and anisotropy of correlated activity on the cortical surface. As σ_R and σ_A increases, correlations decay more slowly with cortical distance along the radial and angular directions, respectively, resulting in a broader spread of correlated activity. The plot shows retinotopic phase maps generated by the model when these parameters are varied around the values used in the main text ($\sigma_R = 1$ and $\sigma_A = 11.5$ in the left hemisphere; $\sigma_R = 1$ and $\sigma_A = 13.0$ in the right hemisphere).